



# The allosteric inhibition of glycine transporter 2 by bioactive lipid analgesics is controlled by penetration into a deep lipid cavity

Received for publication, October 25, 2020, and in revised form, January 6, 2021. Published, Papers in Press, January 12, 2021, <https://doi.org/10.1016/j.jbc.2021.100282>

Katie A. Wilson<sup>1</sup>, Shannon N. Mostyn<sup>2</sup>, Zachary J. Frangos<sup>2</sup>, Susan Shimmon<sup>3</sup>, Tristan Rawling<sup>3</sup>, Robert J. Vandenberg<sup>2</sup>, and Megan L. O'Mara<sup>1,\*</sup>

From the <sup>1</sup>Research School of Chemistry, College of Science, The Australian National University, Canberra, ACT, Australia; <sup>2</sup>Discipline of Pharmacology, School of Medical Sciences, University of Sydney, Sydney, NSW, Australia; <sup>3</sup>School of Mathematical and Physical Sciences, University of Technology Sydney, Sydney, NSW, Australia

Edited by Roger Colbran

The role of lipids in modulating membrane protein function is an emerging and rapidly growing area of research. The rational design of lipids that target membrane proteins for the treatment of pathological conditions is a novel extension in this field and provides a step forward in our understanding of membrane transporters. Bioactive lipids show considerable promise as analgesics for the treatment of chronic pain and bind to a high-affinity allosteric-binding site on the human glycine transporter 2 (GlyT2 or SLC6A5). Here, we use a combination of medicinal chemistry, electrophysiology, and computational modeling to develop a rational structure–activity relationship for lipid inhibitors and demonstrate the key role of the lipid tail interactions for GlyT2 inhibition. Specifically, we examine how lipid inhibitor head group stereochemistry, tail length, and double-bond position promote enhanced inhibition. Overall, the *L*-stereoisomer is generally a better inhibitor than the *D*-stereoisomer, longer tail length correlates with greater potency, and the position of the double bond influences the activity of the inhibitor. We propose that the binding of the lipid inhibitor deep into the allosteric-binding pocket is critical for inhibition. Furthermore, this provides insight into the mechanism of inhibition of GlyT2 and highlights how lipids can modulate the activity of membrane proteins by binding to cavities between helices. The principles identified in this work have broader implications for the development of a larger class of compounds that could target SLC6 transporters for disease treatment.

One in 10 adults worldwide is diagnosed with chronic pain each year (1). Despite the high rate of chronic pain, there is a lack of safe and effective treatment options, which in turn has significant social and economic consequences (2). In the mammalian central nervous system, the neurotransmitter glycine inhibits the pain-signaling pathway (3). Synaptic concentrations of glycine are controlled by the two glycine transporters, GlyT1 and GlyT2, which are responsible for

clearing glycine from synapses (4). GlyT2 is expressed by presynaptic neurons and is also responsible for replenishing presynaptic glycine concentrations to maintain glycinergic neurotransmission. Inhibitors of GlyT2 slow the reuptake of glycine to prolong glycine neurotransmission (5) and have been developed as potential therapeutics in the treatment of chronic pain (6–11).

*N*-acyl amino acids that comprise an amino acid head group conjugated *via* an amide bond to a monounsaturated lipid tail represent a novel class of GlyT2 inhibitors (6). Our previous studies have shown that despite the high level of sequence conservation between GlyT2 and GlyT1, these compounds do not inhibit GlyT1 (6, 12, 13). One of the most promising bioactive lipids from this series, oleoyl *D*-lysine (C18 $\omega$ 9-*D*-Lys), is a selective and potent GlyT2 inhibitor that is metabolically stable, blood–brain barrier permeable, and produces analgesia in a rat model of neuropathic pain with minimal side effects (13). The reduced toxicity of these compounds is attributed to partial inhibition of GlyT2. They reduce but do not completely block glycine transport, which allows presynaptic glycine concentrations to be maintained for subsequent repackaging into synaptic vesicles to maintain glycinergic neurotransmission (14). The most potent bioactive lipids bear positively charged (Lys) or aromatic (Trp) amino acid head groups and inhibit GlyT2 with IC<sub>50</sub> concentrations of less than 50 nM (13). Within the allosteric-binding site, oleoyl-*L*-lysine (C18 $\omega$ 9-*L*-Lys) orients tail down so that the tail intercalates between aliphatic-rich regions of TM5 and TM8 and the oleoyl double bond is in close proximity to TM5 (6). The amino acid head group is accessible to the extracellular solution and stabilized by aromatic residues in TM7, TM8, and EL4 (6).

In the present work, we use a combination of medicinal chemistry, electrophysiology, and computational modeling to explore the structure–activity relationship for lipid inhibitors of GlyT2 to understand how head group stereochemistry and chemical features of the acyl tail affect inhibitor activity and interaction with GlyT2 at a molecular level. The effects of head group stereochemistry are investigated for the most potent previously identified lipid inhibitors, C18 $\omega$ 9-Lys and C18 $\omega$ 9-Trp. To further understand the effect of structure on

This article contains [supporting information](#).

\* For correspondence: Megan L. O'Mara, [megan.omara@anu.edu.au](mailto:megan.omara@anu.edu.au).

## Bioactive lipid inhibitors of glycine transporter 2

inhibitor potency, a series of acyl-lysine analogs were synthesized with variations in the tail length (C18, C16, and C14) and position of the double bond within the lipid tail ( $\omega 9$ ,  $\omega 7$ ,  $\omega 5$ , and  $\omega 3$ ; Fig. 1). Molecular dynamics (MD) simulations were used to provide a structural basis for the effect of chemical changes on lipid inhibitor properties. We demonstrate that the potency of the lipid inhibitors was greatly influenced by a combination of both the stereochemistry of the head group and the length and saturation of the lipid tail. Furthermore, inhibitor potency is shown to depend on deep penetration of the lipid tail into a stabilized location in the allosteric-binding site. This study develops a comprehensive structure–activity relationship for lipid inhibitors of GlyT2. This is critical for future rational design of more effective GlyT2 inhibitors for the treatment of chronic pain and may have broader implications for modulation of other SLC6 transporters.

### Results

#### Head group stereochemistry affects C18 $\omega$ 9-Trp binding but not C18 $\omega$ 9-Lys binding

Bioactive lipids bearing Lys or Trp head groups in the *L*-configurations are among the most potent GlyT2 inhibitors in the series, inhibiting GlyT2 with  $IC_{50}$  concentrations of 25.5 and 54.6 nM, respectively (Table 1). Interestingly, when the head group is converted to the *D*-configuration, the Lys analog (C18 $\omega$ 9-*D*-Lys) retains potency, whereas the Trp analog (C18 $\omega$ 9-*D*-Trp) is inactive (Table 1) (6). To investigate the molecular basis of this activity, MD simulations of 500 ns were performed in triplicate, in which one molecule of either the *L*- or *D*-stereoisomers of C18 $\omega$ 9-Lys or C18 $\omega$ 9-Trp was docked into the extracellular allosteric-binding site of our GlyT2 homology model (15). Only binding poses in which the lipid tail was inserted into the extracellular allosteric-binding site and the double bond was in close proximity to TM5 were considered (6). Regardless of head group amino acid type or stereochemistry, the transporter remains in an outward-occluded conformation (where the intracellular gate distance is  $>4.1$  Å, and the extracellular gate distance is  $<14.0$  Å; Table S1) and the membrane properties are not affected by lipid inhibitor binding (Table S2).

Both C18 $\omega$ 9-*L*-Lys and C18 $\omega$ 9-*D*-Lys remain bound in the allosteric site throughout the combined 1500 ns of MD

simulation with the lipid tail in an extended conformation ( $\sim 17$ – $20$  Å measured from the end of the tail to the stereocenter; Fig. S1), intercalated between TM5, TM7, and TM8 (Figs. 2A and S2). The amino acid head groups remain in close proximity to the protein/bilayer–water interface and interact with the extracellular regions of TM5, TM7, TM8, and EL4, including hydrogen bonding with cationic arginine residues (*i.e.*, R439, R531, and R556) and stacking with nonpolar residues (*i.e.*, F526 and W563). The tail is positioned in a hydrophobic pocket lined by L436, V523, Y550, A553, and F567 (Fig. 2B and C), in agreement with previous studies (6). Interactions that occur with both the head group and tail are sustained for  $>75\%$  of the total simulation time (Table S3). Notably, the more potent inhibitor, C18 $\omega$ 9-*L*-Lys, has deeper penetration into the binding pocket than C18 $\omega$ 9-*D*-Lys. Y550 is a key residue in the interaction of both isomers. Y550 interacts with C18 $\omega$ 9-*L*-Lys above the oleoyl double bond. The change of stereochemistry to C18 $\omega$ 9-*D*-Lys decreases the depth of penetration of the oleoyl tail and shifts the interaction with Y550 below the double bond of C18 $\omega$ 9-*D*-Lys. In this position, the Y550 hydroxyl forms hydrogen bonds with the backbone of W563, so that the lipid tail is sandwiched between Y550 and W563, with W563 interacting directly with the double bond with a CH– $\pi$  interaction. The interactions of Y550 and W563 with both isomers correlate with mutagenesis data reporting that the GlyT2 Y550L and W563L mutants are not inhibited by C18 $\omega$ 9-*L*-Lys or C18 $\omega$ 9-*D*-Lys (6).

In contrast to the lysine-based analogs, the potency of the bioactive lipids bearing Trp head groups is significantly impacted by stereochemistry such that the *D*-isomer is inactive against GlyT2 (Table 1) (6). In MD simulations, C18 $\omega$ 9-*L*-Trp binds to the GlyT2 allosteric site in a similar conformation as C18 $\omega$ 9-*L*-Lys. C18 $\omega$ 9-*L*-Trp is again intercalated between TM5, TM7, and TM8 with the double bond in close proximity to TM5 (Figs. 3A and S3). The *D*-isomer, C18 $\omega$ 9-*D*-Trp, alters its orientation around the stereocenter so the C18 $\omega$ 9 tail points toward EL4, rather than facing the pocket formed by TM5, TM7, and TM8. While C18 $\omega$ 9-*D*-Trp still binds to the GlyT2 extracellular allosteric site, it adopts a much more curled conformation than C18 $\omega$ 9-*L*-Trp ( $\sim 13$  Å *versus*  $\sim 18$  Å measured from the end of the tail to the stereocenter; Fig. S1). This curled conformation results in a shallower binding interaction and reduced depth of penetration of C18 $\omega$ 9-*D*-Trp

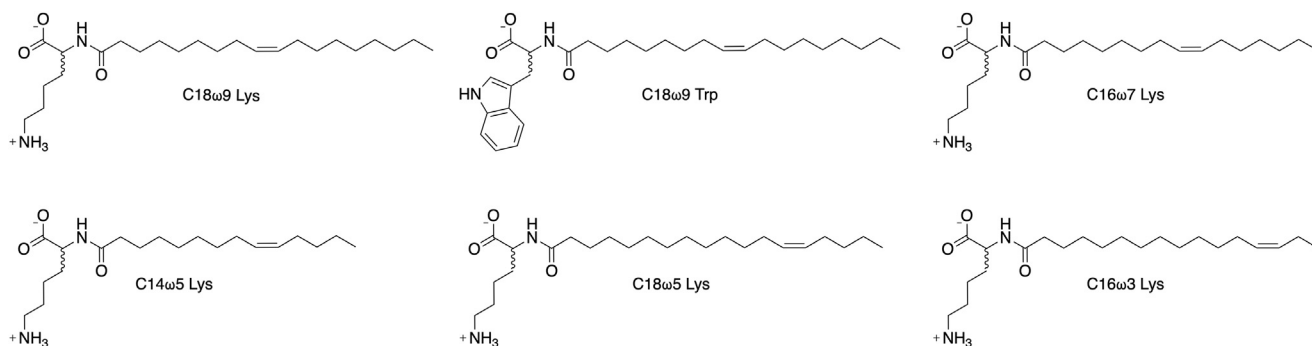


**Figure 1. Chemical structures of GlyT2 lipid inhibitors considered in the present work.** All inhibitors were synthesized as enantiopure *D*- and *L*-isomers.

**Table 1**  
Activity of acyl-lysine analogs at GlyT2 and GlyT1

Inhibitor	L-Head group stereochemistry			D-Head group stereochemistry		
	IC <sub>50</sub> (nM)	% Maximal inhibition	Activity at GlyT1	IC <sub>50</sub> (nM)	% Maximal inhibition	Activity at GlyT1
C18 ω9 Trp	54.6 <sup>a</sup>	86.2 <sup>a</sup>	>10 μM <sup>a</sup>	>10 μM <sup>a</sup>	14.2 <sup>a</sup>	>10 μM <sup>a</sup>
C18ω9 Lys	25.5 <sup>a</sup>	86.8 <sup>a</sup>	>3 μM <sup>a</sup>	48.3 <sup>a</sup>	91.0 <sup>a</sup>	>3 μM <sup>a</sup>
C16ω7 Lys	66.6 (49.9–88.7)	90.2 ± 2.1	>3 μM	602 (373–856)	96.2 ± 2.1	>3 μM
C14ω5 Lys	703 (414–1250)	96.2 ± 7.3	>3 μM	1380 <sup>b</sup>	79.7 ± 3.6	>3 μM
C18ω5 Lys	67.5 (31.7–143)	81.3 ± 5.1	>3 μM	64.9 (36.3–123)	87.6 ± 3.7	>3 μM
C16ω3 Lys	10.8 (8.37–13.8)	94.9 ± 1.6	>3 μM	699 (343–1480)	91.8 ± 8.6	>3 μM

<sup>a</sup> Previously published data from Mostyn *et al.*, 2019 (6).<sup>b</sup> 95% Confidence interval was not able to be calculated. n = 3 to 7 for all measurements.

into the extracellular allosteric site, which alters the coordination of the lipid tail within the binding pocket. Key head group interactions with R439 and F526 were maintained. Residues L436, V523, Y550, A553, and L557 that interact with the lipid tail of C18ω9-D-Lys, C18ω9-L-Lys, and C18ω9-L-Trp instead form interactions with the head group of C18ω9-D-Trp (Fig. 3B and C and Table S3). Only one interaction forms with the C18ω9-D-Trp lipid tail for >75% of the simulation time. Without these key residues stabilizing the position of the acyl tail of C18ω9-D-Trp within the binding site, the tail does not remain bound between TM5, TM7, and TM8 over the course of the MD simulation as observed for the active lipid inhibitors. Instead the lipid tail leaves the allosteric-binding site and reorients in the solution toward EL4, where it adopts a variety of conformations. Despite C18ω9-D-Trp remaining bound in the extracellular allosteric-binding site throughout the total simulation time and the seemingly favorable interaction of the C18ω9-D-Trp head group, no inhibition of GlyT2 is achieved. This indicates that in order for the bioactive lipids to inhibit GlyT2, the tail must be stabilized within the extracellular allosteric-binding site, positioned between TM5, TM7, and TM8. This is in agreement with the inability of free amino acids to cause inhibition (16).

### Shortening the tail of acyl-lysine analogs reduces the depth of penetration and inhibitor potency

The lipid inhibitors described previously contain 18 carbon acyl tails with a *cis*-double bond in the Δ9 position (*i.e.*, nine bonds from the amide linkage to the amino acid head group), and penetration of the lipid tails into the allosteric site appears to be a critical determinant of inhibitory activity. To investigate the effect of tail length on GlyT2 inhibitory activity, we synthesized D- and L-lysine-based inhibitors with truncated tails. Double bonds were maintained in the Δ9 position, and overall chain lengths were reduced to C16 or C14 (C16ω7-Lys and C14ω5-Lys, respectively). The chemical structures of these new lipids are shown in Figure 1, and their synthesis and characterization are described in the Supporting information section. Newly synthesized acyl lysine analogs were then tested against GlyT2 and also tested for selectivity by testing against the closely related GlyT1 transporter using two-electrode voltage clamp electrophysiology (see Table 1 for inhibitory data).

While C18ω9-L-Lys and C18ω9-D-Lys had similar levels of activity, head group conformation greatly affected the

potencies of the chain-shortened analogs. C16ω7-L-Lys inhibited GlyT2 with an IC<sub>50</sub> of 66.6 nM, but the corresponding D-isomer was ninefold less potent (IC<sub>50</sub> of 602 nM; Fig. 4B). Further shortening of the tails to Lys C14ω5 produced a similar preference for L- versus D-, albeit with marked decrease in the potency compared with the C18 analogs (IC<sub>50</sub> concentrations of 770 and 1380 nM for Lys-L-C14ω5 and Lys-D-C14ω5, respectively; Fig. 4D).

To provide a structural explanation of this difference in activity with changing tail length, C16ω7 and C14ω5 acyl lysines in the L- and D-configurations were docked to the extracellular allosteric-binding site, and 500 ns of unrestrained MD simulations were performed in triplicate. Throughout all simulations, GlyT2 remains in an outward-occluded conformation, regardless of the tail length of the acyl lysines (Table S1). The membrane properties are not affected (Table S2).

MD simulations showed that both C16ω7-L-Lys and C14ω5-L-Lys remained bound in the allosteric-binding site throughout the simulation, with the tail positioned between TM5, TM7, and TM8 (Figs. 5A and S4). The Lys head groups of both C16ω7-L-Lys and C14ω5-L-Lys remain in close proximity to the protein/bilayer–water interface, interacting with the extracellular regions of TM5, TM7, TM8, and EL4. C16ω7-L-Lys adopts a similar orientation to that observed for C18ω9-L-Lys, in close proximity to the key binding pocket residues (Fig. 5B and Table S4). As was observed for C18ω9-L-Lys, the C16ω7-L-Lys head group interacts with R436 and F526. Similarly, the L-Lys C16ω7 tail is located between TM5, TM7, and TM8 in the extracellular allosteric-binding site where it interacts with L436, V523, Y550, L557, and F567, and the bottom of the pocket is flanked by V214. As was the case for C18ω9-L-Lys, Y550 interacts with the lipid tail just above the double bond of C16ω7-L-Lys. The similarities between the overall orientation and interactions of C18ω9-L-Lys and C16ω7-L-Lys with key residues in the binding pocket provide a structural basis for the potent inhibition of GlyT2 by both molecules. Further shortening of the lipid tail to give C14ω5-L-Lys significantly reduces the depth of the tail penetration into the binding pocket (Fig. 5A). Furthermore, shortening of the lipid tail dramatically alters C14ω5-L-Lys head group interactions. The C14ω5-L-Lys head group interacts with the membrane, forming hydrogen bonds with 1-palmitoyl-2-oleoyl phosphatidylcholine (POPC) head groups (Fig. S5). There are no

## Bioactive lipid inhibitors of glycine transporter 2

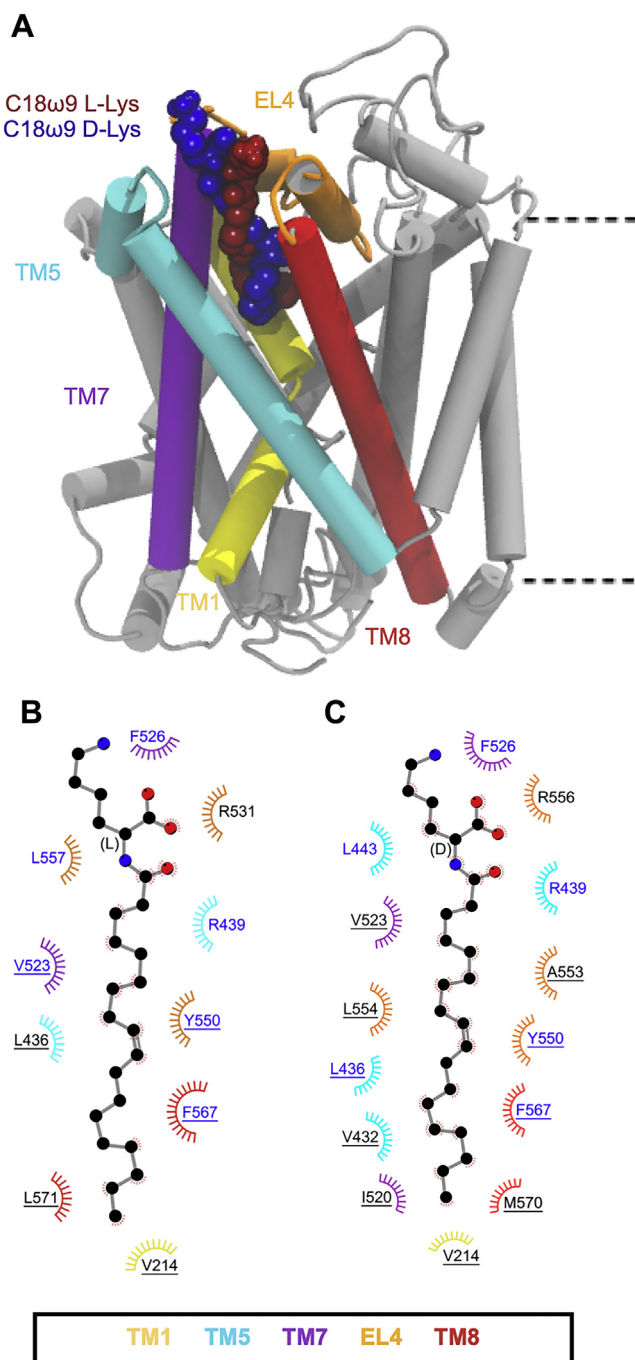


**Figure 2. A**, positions of the Lys C18 $\omega$ 9 lipid inhibitor binding in the extracellular allosteric-binding pocket of GlyT2. **B** and **C**, residues that interact with (B) C18 $\omega$ 9-L-Lys or (C) C18 $\omega$ 9-D-Lys in representative snapshots from molecular dynamics simulations of the lipid inhibitors bound in the allosteric-binding site. Residues that interact with the lipid inhibitor for >75% or <75% of the total simulation time are in blue or black text, respectively. Residues are split based on whether the amino acid interacts with the lipid inhibitor head group (no underline) or tail group (underlined).

interactions with the C14 $\omega$ 5-L-Lys head group that persisted for >75% of the total simulation time (Fig. 5C and Table S4). In contrast, the tail maintains interactions with key residues (*i.e.*, L436, V523, Y550, and F567) for >75% of the total simulation time. In both C14 $\omega$ 5-L-Lys and C16 $\omega$ 7-L-Lys, the tail only penetrates as deep as F567 (Fig. 5, B and C), which

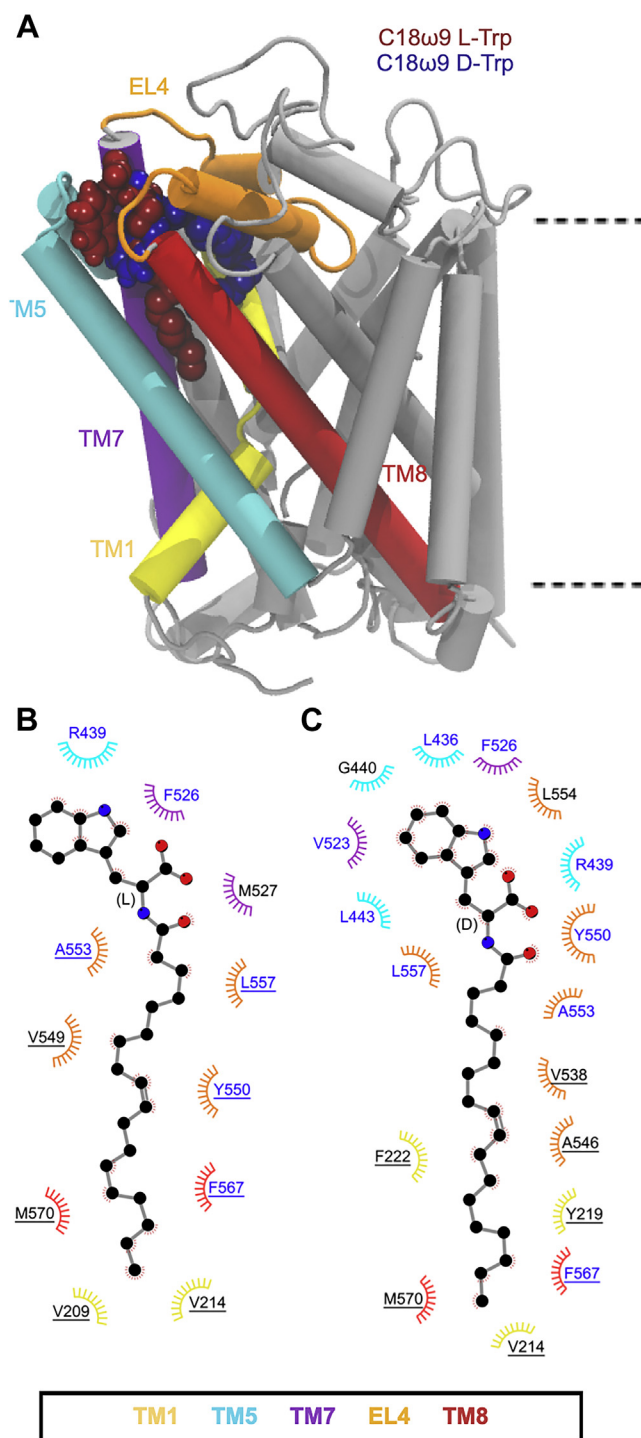


**Figure 3. A**, position of the two Trp C18 $\omega$ 9 lipid inhibitors in the extracellular allosteric-binding pocket of GlyT2. **B** and **C**, residues that interact with (B) C18 $\omega$ 9-L-Trp or (C) C18 $\omega$ 9-D-Trp in representative snapshots from molecular dynamics simulations of the lipid inhibitors bound in the allosteric-binding site. Residues that interact with the lipid inhibitor for >75% or <75% of the total simulation time are highlighted in blue or black, respectively. Residues are split based on whether the amino acid interacts with the lipid inhibitor head group (no underline) or tail group (underlined).

interacts with C6 of C18 $\omega$ 9-L-Lys and C5 of C16 $\omega$ 7-L-Lys. This change in orientation of C14 $\omega$ 5-L-Lys ( $IC_{50}$  of 703 nM) relative to C16 $\omega$ 7-L-Lys ( $IC_{50}$  of 66.6 nM) and C18 $\omega$ 9-L-Lys

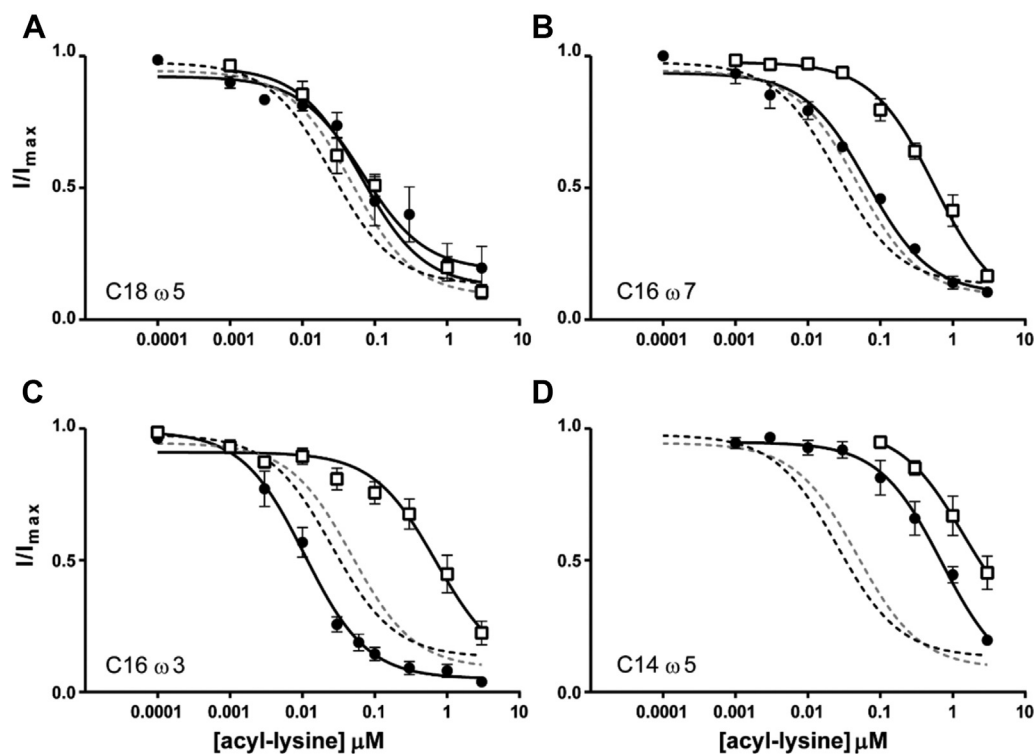


**Figure 4. Inhibitory activity of acyl-lysine analogs at GlyT2.** Increasing concentrations of acyl lysine compounds were applied to oocytes expressing WT GlyT2 transporters. The transport current at each concentration is normalized to the current produced by 30  $\mu\text{M}$  glycine in the absence of inhibitor. For each panel, the L-isomer is represented by *black circles*, and the D-isomer is shown as *open squares*. The curve fits for oleoyl (C18 $\omega$ 9) lysine are also shown as *black* (L-) and *gray* (D-) dashed lines for comparison. A, C18 $\omega$ 5 acyl-lysine. B, C16 $\omega$ 7 acyl-lysine. C, C16 $\omega$ 3 acyl-lysine. D, C14 $\omega$ 5 acyl-lysine. See Table 1 for  $\text{IC}_{50}$  values, 95% confidence interval, and sample sizes.

( $\text{IC}_{50}$  of 25.5 nM) correlates with the dramatic decrease in GlyT2 inhibition observed for C14 $\omega$ 5-L-Lys.

On change of stereochemistry to the D-configuration, C16 $\omega$ 7-D-Lys and C14 $\omega$ 5-D-Lys only remain bound in the extracellular allosteric site for approximately one third ( $\sim 500$  ns) of the total simulation time. This is in contrast to C18 $\omega$ 9-D-Lys, which remains bound throughout the entire simulation. Furthermore, C16 $\omega$ 7-D-Lys and C14 $\omega$ 5-D-Lys adopt a different conformation in the extracellular allosteric-binding pocket to C18 $\omega$ 9-D-Lys (Figs. 6A and S6). Specifically, the C16 $\omega$ 7-D-Lys head group interacts with the head groups of membrane POPC lipids (Fig. S4B) while maintaining interactions with key GlyT2 residues (F526, R439, and R556; Fig. 6B and Table S4). While the C16 $\omega$ 7-D-Lys tail group is positioned in the extracellular allosteric-binding pocket in a similar orientation to C18 $\omega$ 9-D-Lys and interacts with L436, V523, Y550, and F567, none of these interactions persist for  $>75\%$  of the total simulation time (Fig. 6B and Table S4). The reduced occupancy and different binding orientation of C16 $\omega$ 7-D-Lys ( $\text{IC}_{50}$  of 602 nM) in the extracellular allosteric-binding site in part explain the 12-fold reduced potency relative to C18 $\omega$ 9-D-Lys ( $\text{IC}_{50}$  of 48.3 nM). In the case of C14 $\omega$ 5-D-Lys, the D-Lys head group interacts with F526 and R439 in a similar manner to C18 $\omega$ 9-D-Lys. However, the C14 $\omega$ 5-D-Lys tail protrudes into the surrounding membrane where it interacts with POPC at the protein-lipid interface (Fig. S7). In this orientation, L443 is the only key residue interacting with the lipid tail for  $>75\%$  of the total simulation time (Fig. 6C). The lack of interactions and reduced occupancy in the extracellular allosteric-binding site may in part explain why

C14 $\omega$ 5-D-Lys is not an effective inhibitor of GlyT2 ( $\text{IC}_{50}$  of 1380 nM).

#### The position of the double bond in the lipid tail changes the activity of acyl-lysine analogs

To assess the effect of the double-bond position on activity, we synthesized C18 $\omega$ 5-Lys and C16 $\omega$ 3-Lys, which contain *cis*-double bonds in the  $\Delta 13$  position (Fig. 1). Both L- and D-isomers of C18 $\omega$ 5-Lys inhibit GlyT2 with  $\text{IC}_{50}$  concentrations of 67.5 and 64.9 nM, respectively (Fig. 4A and Table 1). This trend is consistent with the results for C18 $\omega$ 9-L-Lys and C18 $\omega$ 9-D-Lys, where the configuration of the amino acid head group did not greatly alter the activity. However, when the length of the acyl chain was decreased to C16, the position of the double bond produced a marked difference in inhibitory activity between isomers. Thus, C16 $\omega$ 3-L-Lys is a potent inhibitor of GlyT2 ( $\text{IC}_{50}$  of 10.8 nM), whereas the corresponding D-isomer was 65-fold less potent, with an  $\text{IC}_{50}$  of 699 nM (Fig. 4C).

To provide a structural explanation of this difference in activity with changing tail length, the L- and D-isomers of C18 $\omega$ 5 and C16 $\omega$ 3 Lys were docked to the extracellular allosteric-binding pocket and simulated for 500 ns in triplicate. Regardless of the presence of a bound inhibitor, GlyT2 again remains in an outward-occluded conformation (Table S1) throughout the simulations, and the membrane properties are not affected (Table S2). Both stereoisomers with C18 tails (C18 $\omega$ 5-L-Lys and C18 $\omega$ 5-D-Lys) remained bound in the

## Bioactive lipid inhibitors of glycine transporter 2

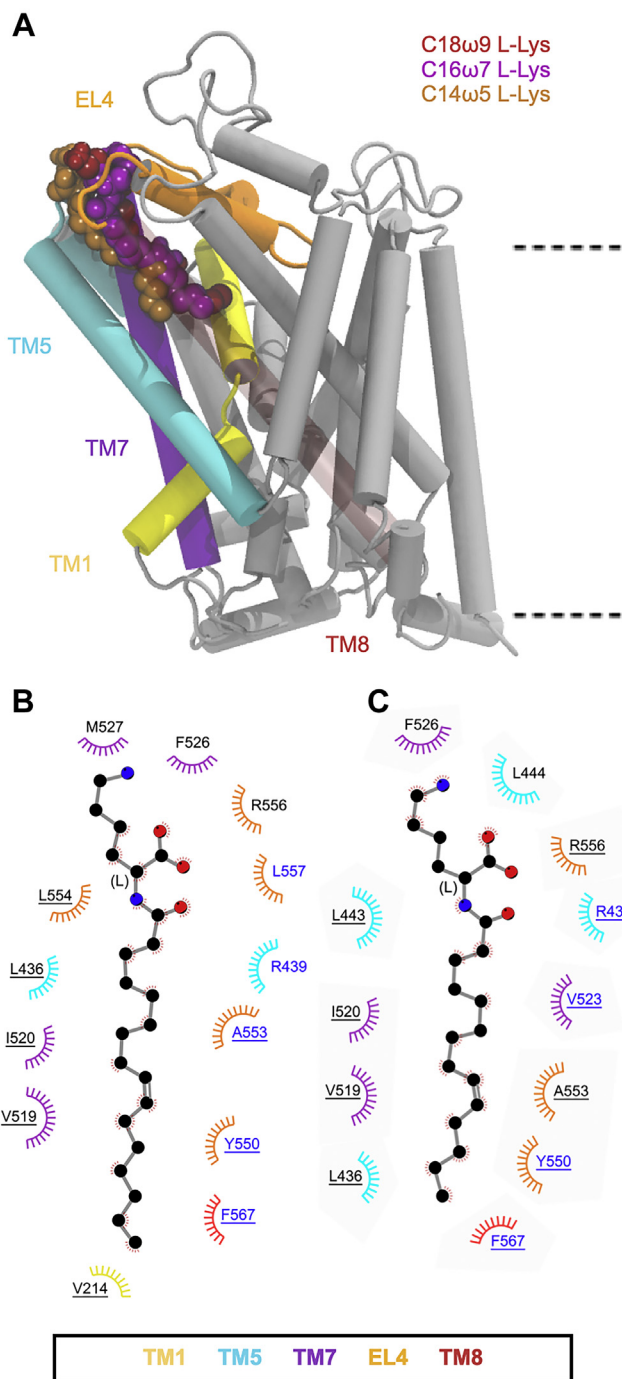


**Figure 5. A**, positions of the L-Lys C18 $\omega$ 9, C16 $\omega$ 7, and C14 $\omega$ 5 lipid inhibitor binding in the extracellular allosteric-binding pocket of GlyT2. TM8 is transparent for clarity. **B** and **C**, residues that interact with C16 $\omega$ 7-L-Lys (**B**) or C14 $\omega$ 5-L-Lys (**C**) in representative snapshots from molecular dynamics simulations of the lipid inhibitors bound in the allosteric-binding site. Residues that interact with the lipid inhibitor for >75% or <75% of the total simulation time are in blue or black text, respectively. Residues are split based on whether the amino acid interacts with the lipid inhibitor head group (no underline) or tail group (underlined).

allosteric pocket throughout all simulations. The overall binding conformation and potencies of C18 $\omega$ 5-L-Lys and C18 $\omega$ 5-D-Lys were similar to that of the C18 $\omega$ 9-L-Lys and C18 $\omega$ 9-D-Lys (Fig. 7A). The head group interactions with F526, L443, and R439 are maintained (Figs. 7B and C and S8 and

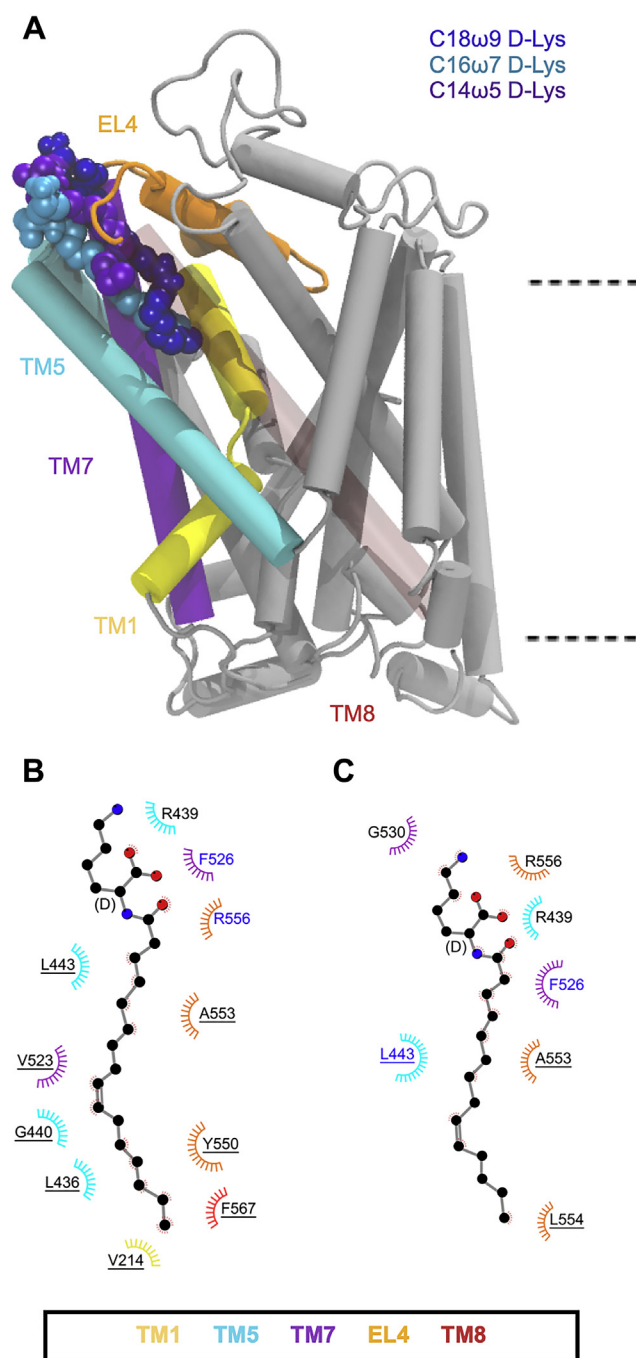


**Figure 6. A**, positions of the D-Lys C18 $\omega$ 9, C16 $\omega$ 7, and C14 $\omega$ 5 lipid inhibitor binding in the extracellular allosteric-binding pocket of GlyT2. For clarity, TM8 is transparent. **B** and **C**, residues that interact with C16 $\omega$ 7-D-Lys (**B**) or C14 $\omega$ 5-D-Lys (**C**) in representative snapshots from molecular dynamics simulations of the lipid inhibitors bound in the allosteric-binding site. Residues that interact with the lipid inhibitor for >75% or <75% of the total simulation time are in blue or black text, respectively. Residues are split based on whether the amino acid interacts with the lipid inhibitor head group (no underline) or tail group (underlined).

Table S5), and the tails of C18 $\omega$ 5-L/D-Lys are located between TM5, TM7, and TM8, interacting with the nonpolar residues (e.g., V214, L436, Y550, L557, and F567) and Y550 interacts with the lipid tail above the double bond (Fig. 7), giving a structural basis for their activity.

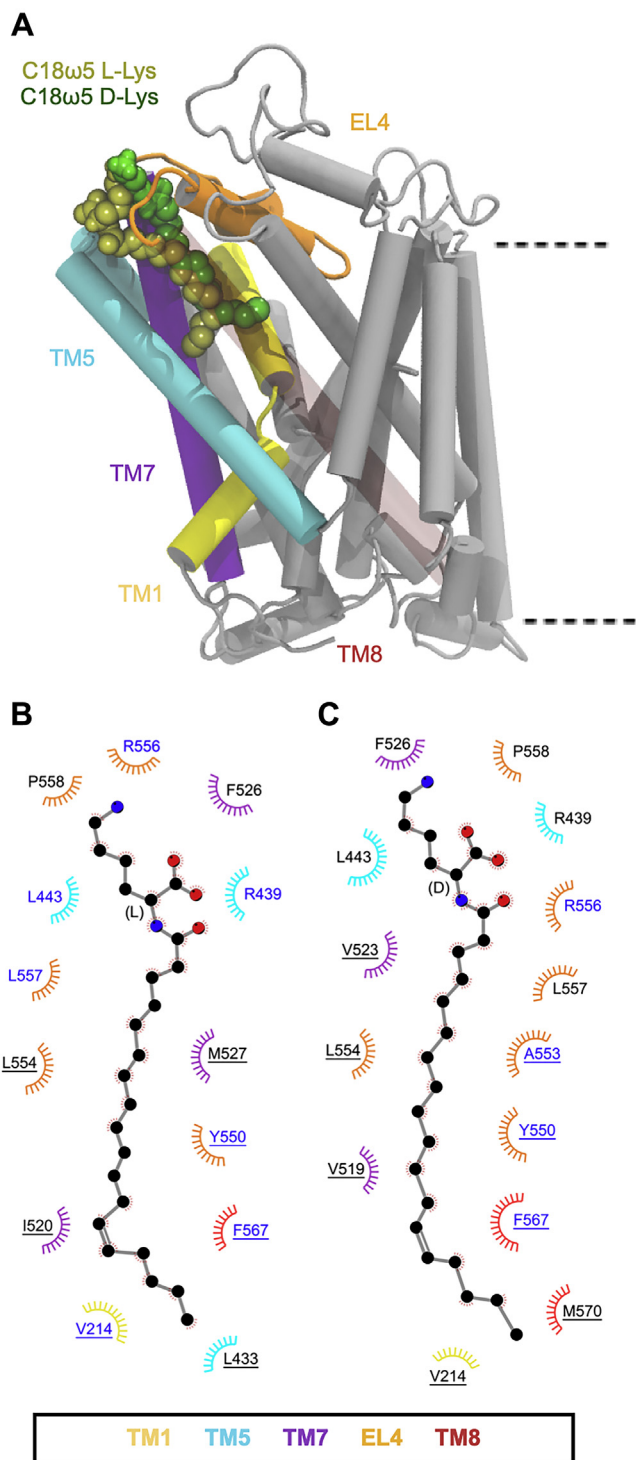


**Figure 7. A, positions of the C18 $\omega$ 9 L-Lys, C18 $\omega$ 5 L-Lys, and C18 $\omega$ 5 D-Lys lipid inhibitor binding in the extracellular allosteric-binding pocket of GlyT2.** For clarity, TM8 is transparent. **B** and **C**, residues that interact with C18 $\omega$ 5 L-Lys (**B**) or C18 $\omega$ 5 D-Lys (**C**) in representative snapshots from molecular dynamics simulations of the lipid inhibitors bound in the allosteric-binding site. Residues that interact with the lipid inhibitor for >75% or <75% of the total simulation time are in blue or black text, respectively. Residues are split based on whether the amino acid interacts with the lipid inhibitor head group (no underline) or tail group (underlined).

Major differences in the binding interactions of the C16 isomers were observed, consistent with their IC<sub>50</sub> concentrations. C16 $\omega$ 3-L-Lys, the most potent inhibitor of GlyT2 in this lipid series, remains bound in the allosteric pocket throughout the combined MD simulations, whereas C16 $\omega$ 3-D-Lys only remains bound in the extracellular allosteric-binding pocket for approximately one-third of the total simulation time. In the case of C16 $\omega$ 3-L-Lys, the head group interacts with F526, L443, and R439, as observed for C18 $\omega$ 9-L-Lys (Figs. 8 and S9). Unlike other inhibitory lipids, the C16 $\omega$ 3-L-Lys tail does not adopt an extended conformation but instead has a curled conformation in the allosteric-binding site between TM5, TM7, and TM8. The curled C16 $\omega$ 3-L-Lys tail interacts with W215, Y550, L557, F567, and L436 (Fig. 8B and Table S5). The interaction between C16 $\omega$ 3-L-Lys and W215 is unique and notable because W215 is directly adjacent to the glycine-binding site and physically separates the extracellular allosteric site and the vestibular substrate-binding site. Interactions with W215 may reflect communication between the extracellular allosteric-binding site and the vestibular substrate-binding site. This altered orientation and the interaction with W215 may in part explain why C16 $\omega$ 3-L-Lys is the most potent lipid inhibitor identified to date. In contrast, the potency of C16 $\omega$ 3-D-Lys is 65-fold lower (IC<sub>50</sub> of 699 nM) than C16 $\omega$ 3-L-Lys. Simulations of C16 $\omega$ 3-D-Lys in the extracellular allosteric-binding site show that the head group interacts with the membrane as well as key amino acids (*i.e.*, R439 and F526, Fig. 8C). The tail does not bind stably in the allosteric-binding pocket between TM5, TM7, and TM8 but instead is oriented toward EL4 interacting with L557 and L436, and it readily dissociates from the binding site.

**Nonpolar residues stabilize lipid inhibitor binding, while the stabilizing or destabilizing effect of cationic residues depends on the lipid inhibitor head group**

The binding affinity of lipid inhibitors to the allosteric-binding pocket of GlyT2 is influenced by both the amino acid head group and the depth of penetration of the lipid tail. To better understand the overall energetics of lipid inhibitor binding, the contribution of each amino acid to the relative binding energy was calculated using the molecular mechanics Poisson-Boltzmann surface area energy decomposition scheme. The focus was placed on binding of the most potent lipid inhibitor, C16 $\omega$ 3-L-Lys. Twenty-three residues were identified as having a contribution of more than -1 kJ/mol to C16 $\omega$ 3-L-Lys binding. Twenty of these were nonpolar, and three were polar (Thr442, Glu536, and Glu459). The polar residues contributed up to -2.0 kJ/mol to C16 $\omega$ 3-L-Lys binding. Residues that have the greatest energetic impact on binding stability are I520 (-4.9 kJ/mol), V519 (-4.7 kJ/mol), F567 (-4.5 kJ/mol), L557 (-4.5 kJ/mol), L443 (-4.4 kJ/mol), V523 (-4.4 kJ/mol), and L436 (-4.3 kJ/mol; Fig. 9). With the exception of V519, these residues are all within 4 Å of C16 $\omega$ 3-

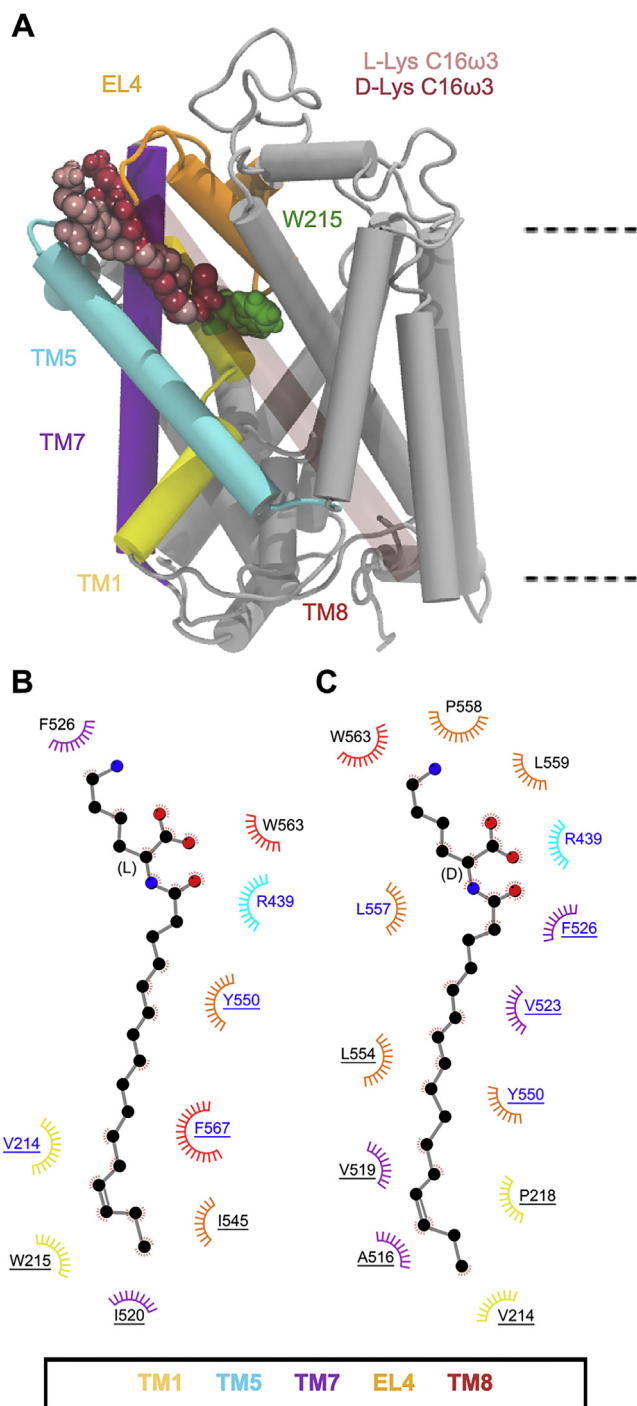


**Figure 8. A, positions of the C16 $\omega$ 7 L-Lys, C16 $\omega$ 3 L-Lys, and C16 $\omega$ 3 D-Lys lipid inhibitor binding in the extracellular allosteric-binding pocket of GlyT2.** For clarity, TM8 is transparent. **B** and **C**, residues that interact with C16 $\omega$ 3 L-Lys **B** or C16 $\omega$ 3 D-Lys **C** in representative snapshots from molecular dynamics simulations of the lipid inhibitors bound in the allosteric-binding site. Residues that interact with the lipid inhibitor for >75% or <75% of the total simulation time are in blue or black text, respectively. Residues are split based on whether the amino acid interacts with the lipid inhibitor head group (no underline) or tail group (underlined).

L-Lys for >80% of the total simulation time (Table S5) and are mostly located around the lipid tail (Fig. 9C). All residues that destabilize binding by more than 1.2 kJ/mol are cationic, whereas all other residues that destabilize binding by 0.1 kJ/

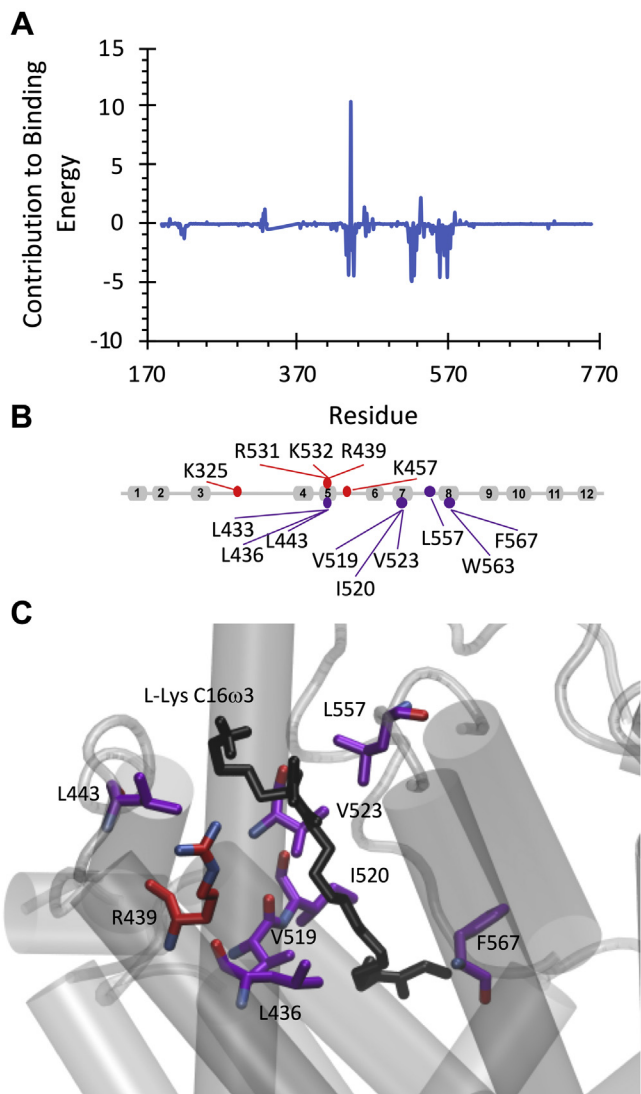


**Figure 9. A, energetic contribution (MM-PBSA, kJ/mol) of GlyT2 residues to C16 $\omega$ 3 L-Lys binding. B, residues that destabilize the complex by >1.2 kJ/mol or residues that stabilize the binding by >2.5 kJ/mol. C, position of residues that destabilize the complex by >5.0 kJ/mol or residues that stabilize the binding by >5.0 kJ/mol relative to the C16 $\omega$ 3 L-Lys lipid inhibitor.**

mol are charged. R439 is the residue that most significantly destabilizes binding (10.5 kJ/mol) because of charge repulsion between the C16 $\omega$ 3-L-Lys head group and the R439 side chain.

To give insight into the effect of the inhibitor structure on the activity, the overall energetics of C18 $\omega$ 9-L-Lys and C18 $\omega$ 9-L-Trp binding were also calculated (Fig. 10). The two most potent inhibitors, C18 $\omega$ 9-L-Lys and C16 $\omega$ 3-L-Lys, have very similar binding energy decompositions, with nonpolar residues (V523, L436, I520, F526, and L557) stabilizing binding and charged amino acid destabilizing binding (R439). Head group substitution to C18 $\omega$ 9-L-Trp dramatically alters the per-residue decomposition of the binding energy. All residues that strongly stabilize C18 $\omega$ 9-L-Trp binding are cationic (R556, R531, K532, K325, R439, K323, and K321), and all strongly destabilizing residues are anionic (E372, D329, E552, D322, and E530). All these residues are positioned on the



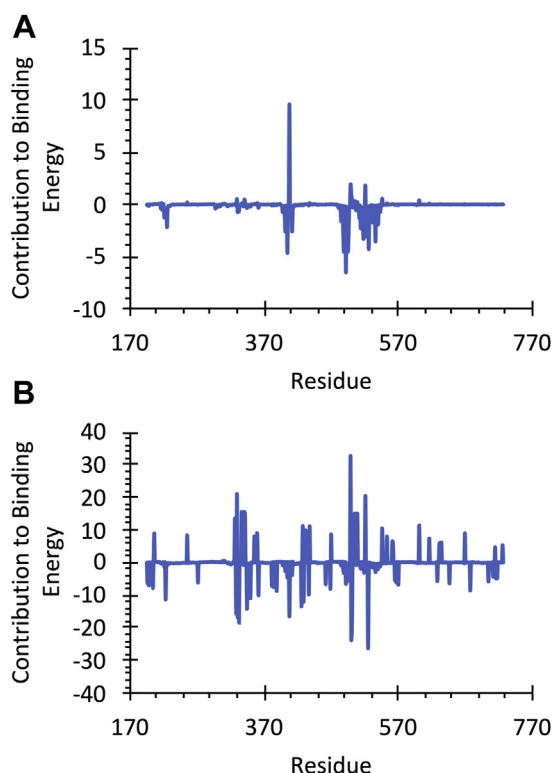


**Figure 10.** Energetic contribution (MM-PBSA, kJ/mol) of GlyT2 residues to (A) C18 $\omega$ 9-L-Lys and (B) C18 $\omega$ 9-L-Trp binding.

extracellular surface of protein surrounding the C18 $\omega$ 9-L-Trp head group. Interestingly, the overall binding energy for C18 $\omega$ 9-L-Trp ( $-218.89 \pm 25.8$  kJ/mol) is greater than that for the acyl lysine inhibitors ( $-104.5 \pm 21.5$  and  $-110.9 \pm 29.5$  kJ/mol for C16 $\omega$ 3-L-Lys and C18 $\omega$ 9-L-Lys, respectively). This result highlights that while both acyl lysine and acyl tryptophan inhibitors can act on GlyT2, the biochemical basis of inhibitor stabilization in the extracellular allosteric-binding site differs between compounds.

## Discussion

The present work has highlighted that whilst interactions between GlyT2 and the lipid head group occur, it is the interactions with the lipid tail that are critical for determining the activity of the lipid inhibitor. This may form the basis for the potential mechanism of inhibition. The high sequence conservation of the extracellular allosteric-binding site residues across SLC6 transporters suggests that this lipid-binding interaction could be exploited for broader inhibitor design. The position of the tail in between TM5, TM7, TM8, and EL4 spans both the core domain of the transporter (TM1, TM2, TM6, TM6, and TM7) and the scaffold domain (TM3, TM4, TM8, and TM9) (17, 18) and may disrupt the rocking bundle mechanism of glycine transport. Indeed, the transition between the outward-occluded state and inward-open state in the homologous protein LeuT has been shown to involve substantial conformational change causing the bending of TM5 and TM7 and the closure of the central vestibule by EL4 (17, 18). MD simulations of the dopamine transporter and

serotonin transporter have also identified changes in TM5 as a first step in this conformational transition (19). To further explore the impact the inhibitors are having on the overall protein structure, the hydrogen bonds between each of the transmembrane helices over the simulations were recorded. While most interhelical interactions remain undisrupted (*i.e.*, TM6–TM2, TM2–TM7, TM3–TM10, TM10–TM11), notable differences are observed in the interhelical interactions when active lipid inhibitors are bound (Table S5). In the extracellular allosteric-binding pocket, TM5 and TM7 interact through a hydrogen bond between Y430(OH) and T512(O $\gamma$ ). This interaction is lost when the active lipid inhibitors are bound but are undisturbed relative to the control when the inactive C18 $\omega$ 9-D-Trp is bound. This change in hydrogen bonding between TM5 and TM7 may be able to modulate the conformational change required for substrate transport. The conformations of the extracellular loops and thereby closure of the central vestibule were also examined. The binding of the lipid inhibitors changes the conformation of EL4, which in turn changes how EL4 interacts with the other extracellular loops. While the interaction between EL4 and EL2 as well as EL2 and EL6 is preserved, the interaction between EL4 and EL6 is disrupted when active lipid inhibitors are bound (Fig. S10). This in turn leads to the loss of a hydrogen bond in the vicinity of EL6 on the extracellular edges of TM10 (Y627 or Q630) and TM12 (Y710) and a widening of the gap between EL4 and EL6, which opens up the central vestibule. This is the first evidence of allosteric conformational changes induced by lipid inhibitor binding to GlyT2.

In the present work, we have investigated the impact of head group stereochemistry and acyl tail structure on the activity of lipid-based inhibitors of GlyT2. Overall, the lipid inhibitor head groups remain stabilized in the aromatic cage formed by R439, F526, W563, and R556, whereas the tail group penetrated into the cavity to different depths, depending on inhibitor tail length and double-bond position. Importantly, longer tail lengths and deeper binding correlated with increased activity. The most potent inhibitor, C16 $\omega$ 3-L-Lys, has unique interactions with W215, which is positioned between the extracellular allosteric-binding site and substrate-binding site. C16 $\omega$ 3-L-Lys has a potency that is similar to that of the most potent small molecule GlyT2 inhibitor to date (ORG25543; IC $_{50}$  = 16 nM). The order of potency of the remaining inhibitors is C18 $\omega$ 9-L-Lys > C18 $\omega$ 9-L-Trp, C18 $\omega$ 9-D-Lys, C16 $\omega$ 7-L-Lys, C18 $\omega$ 5-L-Lys, C18 $\omega$ 5-D-Lys > C16 $\omega$ 7-D-Lys, C16 $\omega$ 3-D-Lys, C14 $\omega$ 5-L-Lys > C14 $\omega$ 5-D-Lys >>> C18 $\omega$ 9-D-Trp. We have shown that the energetic stabilization of acyl lysine and acyl tryptophan inhibitors in the extracellular allosteric-binding site varies significantly, that overall the L-stereoisomer is typically more potent than the D-stereoisomer, and the position of the double bond influences the activity of the inhibitor. We propose that the formation of this deep binding pocket is critical for inhibition, and that bioactive lipids that can penetrate the aliphatic cavity of the extracellular allosteric-binding site are superior inhibitors. Furthermore, this provides insight into the mechanism of inhibition of GlyT2 and

## Bioactive lipid inhibitors of glycine transporter 2

highlights how lipids can modulate the activity of membrane proteins by infiltrating pockets between helices, a phenomenon that has been similarly proposed in cannabinoid receptors and cys-loop receptors (20–23). The present work has provided insight into the structural features of GlyT2 inhibitors that will be important for the future design of novel inhibitors of GlyT2. The structural basis of inhibitor activity reported here may provide insights that are applicable to the broader development of new compounds that could target homologous neurotransmitter transporters, such as the dopamine, serotonin, and noradrenaline transporters.

### Experimental procedures

All *N*-acyl amino acids were synthesized as previously described (13). See [Supporting Information](#) for full details. Stock solutions of 10 mg ml<sup>-1</sup> of *N*-acyl amino acids were dissolved in dimethyl sulfoxide and diluted in frog Ringer's solution (96 mM NaCl, 2 mM KCl, 1 mM MgCl<sub>2</sub>, 1.8 mM CaCl<sub>2</sub>, 5 mM Hepes, pH 7.5) to desired concentrations. Final solutions contained 0.0025% dimethyl sulfoxide, a concentration that had no effect on transporter or receptor function.

### WT and mutant RNA transcription

Human GlyT2a WT complementary DNA was subcloned into the plasmid oocyte transcription vector. The amplified GlyT2/plasmid oocyte transcription vector product was then transformed in *Escherichia coli* cells and subsequently purified using the PureLink Quick Plasmid Miniprep Kit (Invitrogen by Life Technologies) and sequenced by the Australian Genome Research Facility (Sydney, Australia). The purified plasmid DNA was linearized *via* the restriction enzyme, SpeI (New England Biolabs [Genesearch]) for GlyT2a. Complementary RNAs were synthesized using the mMESAGE mMACHINE T7 kit (Ambion).

### Oocyte preparation and injection

All work involving the use of animals was performed in accordance with the Australian Code of Practice for the Care and Use of Animals for Scientific Purposes. *Xenopus laevis* frogs (NASCO) were anesthetized with 0.17% (w/v) 3-amino-benzoic acid ethyl ester and had an ovarian lobe removed *via* an incision in the abdomen. Stage V oocytes were isolated from the lobe *via* digestion with 2 mg ml<sup>-1</sup> collagenase A (Boehringer) at 26 °C for 1 h, and 20 ng of cRNA encoding GlyT2 was injected into each oocyte cytoplasm (Drummond Nanoinject; Drummond Scientific Co). The oocytes were then stored in frog Ringer's solution (96 mM NaCl, 2 mM KCl, 1 mM MgCl<sub>2</sub>, 1.8 mM CaCl<sub>2</sub>, 5 mM Hepes, pH 7.5), which was supplemented with 2.5 mM sodium pyruvate, 0.5 mM theophylline, 50 µg/ml gentamicin and 100 µM ml<sup>-1</sup> tetracycline. The oocytes were stored at 18 °C for 3 to 5 days, until transporter expression was adequate for measurement using the two-electrode voltage clamp technique. Adequate transporter expression was defined as a ≥30 nA current following application of the glycine EC<sub>50</sub>.

### Two-electrode voltage clamp electrophysiology

GlyT2 is electrogenic, allowing activation to be measured *via* the two-electrode voltage clamp technique. Oocytes were voltage clamped at -60 mV, and whole-cell currents generated by the substrate were recorded with a Geneclamp 500 amplifier (Axon Instruments), digitized by a Powerlab 2/20 chart recorder (ADInstruments). LabChart version 8 software (ADInstruments, Axon Instruments) was used to visualize and process current traces. Recordings were performed in frog Ringer's solution. Oocytes were placed in an oval-shaped bath with a volume of 0.3 ml, with laminar flow around the oocyte at a rate of 12 ml min<sup>-1</sup> under gravity feed.

Each of the synthesized acyl-lysine compounds were first tested for their inhibitory activity by coapplying the analogs with 30 µM glycine and assessing their ability to reduce glycine transport currents. Increasing concentrations of each acyl-lysine inhibitor were applied to generate concentration response curves, from which IC<sub>50</sub> values and percent maximal inhibition values were calculated. Acyl-lysines were also applied to the related transporter GlyT1 to assess their selectivity and were shown to not significantly inhibit GlyT1 currents at concentrations up to 3 µM. We previously showed that concentrations of up to 3 µM of oleoyl L-lysine do not alter uninjected oocytes, and that the critical micelle concentration of positively charged bioactive lipids is above this value (13).

### Computational modeling

Docking and MD simulations were performed using the protocol developed in our previous work (6). Briefly, each of the lipid inhibitors was docked to our previously validated GlyT2 homology model using Autodock vina (24). The lipids were treated in a united atom representation to be consistent with the subsequent MD simulations and treated as flexible. Lipid inhibitors were docked to the previously identified extracellular allosteric-binding pocket. Following docking, the pose with the lipid inhibitors bound with the tail inserted into the extracellular pocket and the double bond in close proximity to TM5 and the protein–lipid interface was considered for simulation.

The Automated Topology Builder and Repository (25) was used to develop united atom coordinates and parameters for the lipid inhibitors (Molecule IDs: 252930, 340331, 252919, 253354, 364924, 364925, 364971, and 364972). To ensure that there was no isomerization around the *cis*-double bond, the force constant related to this dihedral angle in the lipid inhibitors was adjusted from 5.86 to 41.80 kJ mol<sup>-1</sup> rad<sup>-2</sup>. The protonation state for all lipids was that in which it would most likely be found at physiological pH (pH 7): POPC and the lipid inhibitors with a Lys head group were zwitterions, whereas the lipid inhibitors with a Trp head group were deprotonated. The simulations were performed using GROMACS, version 2016.1 (26), with the GROMOS 54A7 force field for lipids and proteins (27). GlyT2 was embedded in a membrane containing 80% POPC and 20% cholesterol, each system was neutralized, and salt was added to a concentration of

0.15 M NaCl. All systems were minimized using a steepest descent and equilibrated with decreasing restraints on the protein in five sequential 1 ns simulations (1000 kJ mol<sup>-1</sup> nm<sup>-2</sup>, 500 kJ mol<sup>-1</sup> nm<sup>-2</sup>, 100 kJ mol<sup>-1</sup> nm<sup>-2</sup>, 50 kJ mol<sup>-1</sup> nm<sup>-2</sup>, and 10 kJ mol<sup>-1</sup> nm<sup>-2</sup>). Each system was then simulated without constraints in triplicate for 500 ns. Throughout all simulations, the pressure was maintained at 1 bar using semi-isotropic position scaling and the Berendsen barostat ( $\tau_P = 0.5$  ps and isothermal compressibility =  $4.5 \times 10^{-5}$  bar), the temperature was maintained at 300 K using the Bussi–Donadio–Parrinello velocity rescale thermostat ( $\tau_P = 0.1$  ps), the periodic boundary condition, a 2 fs time step, SETTLE was used to constrain the geometry of water molecules, and LINCS was used to constrain the covalent bond lengths of the solute. Visualization of the simulations was performed using the Visual Molecular Dynamics software (28). Analysis was done on frames spaced by 0.1 ns using gromacs tools and Visual Molecular Dynamics software.

### Data availability

All experimental data are contained within the article, whereas computational data are available from [https://github.com/OMaraLab/GlyT2\\_SAR](https://github.com/OMaraLab/GlyT2_SAR).

**Acknowledgments**—This work was supported by a grant from the National Health and Medical Research Council (APP1144429). This research was undertaken with the assistance of resources and services from the National Computational Infrastructure, which is supported by the Australian Government; and the Pawsey Supercomputing Centre, which is supported by the Australian Government and the Government of Western Australia.

**Author contributions**—K. A. W., S. N. M., R. J. V., and M. L. O. designed the research; K. A. W. performed the simulations; S. N. M. and Z. J. F. performed the electrophysiology; S. S. and T. R. synthesized the inhibitors; K. A. W., S. N. M., and Z. J. F. contributed to the analysis; K. A. W., S. N. M., Z. J. F., T. R., R. J. V., and M. L. O. drafted the paper; K. A. W., S. N. M., Z. J. F., S. S., T. R., R. J. V., and M. L. O. have given their final approval to this version of the manuscript.

**Conflict of interest**—The authors declare that they have no conflicts of interest with the contents of this article.

**Abbreviations**—The abbreviations used are: C18 $\omega$ 9-D-Lys, oleoyl-D-lysine; C18 $\omega$ 9-L-Lys, oleoyl-L-lysine; GlyT, glycine transporter; MD, molecular dynamics; POPC, 1-palmitoyl-2-oleoyl phosphatidylcholine.

### References

- Goldberg, D. S., and McGee, S. J. (2011) Pain as a global public health priority. *BMC Public Health* **11**, 770
- Volkow, N., Benveniste, H., and McLellan, A. T. (2018) Use and misuse of opioids in chronic pain. *Annu. Rev. Med.* **69**, 451–465
- Todd, A. J. (2010) Neuronal circuitry for pain processing in the dorsal horn. *Nat. Rev. Neurosci.* **11**, 823–836
- Eulenburg, V., Armsen, W., Betz, H., and Gomeza, J. (2005) Glycine transporters: Essential regulators of neurotransmission. *Trends Biochem. Sci.* **30**, 325–333
- Cioffi, C. L. (2018) Modulation of glycine-mediated spinal neurotransmission for the treatment of chronic pain. *J. Med. Chem.* **61**, 2652–2679
- Mostyn, S. N., Wilson, K. A., Schumann-Gillett, A., Frangos, Z. J., Shimmon, S., Rawling, T., Ryan, R. M., O'Mara, M. L., and Vandenberg, R. J. (2019) Identification of an allosteric binding site on the human glycine transporter, GlyT2, for bioactive lipid analgesics. *Elife* **8**, e47150
- Caulfield, W. L., Collie, I. T., Dickens, R. S., Epemolu, O., McGuire, R., Hill, D. R., McVey, G., Morphy, J. R., Rankovic, Z., and Sundaram, H. (2001) The first potent and selective inhibitors of the glycine transporter type 2. *J. Med. Chem.* **44**, 2679–2682
- Takahashi, E., Arai, T., Akahira, M., Nakajima, M., Nishimura, K., Omori, Y., Kumagai, H., Suzuki, T., and Hayashi, R. (2014) The discovery of potent glycine transporter type-2 inhibitors: Design and synthesis of phenoxymethylbenzamide derivatives. *Bioorg. Med. Chem. Lett.* **24**, 4603–4606
- Vandenberg, R. J., Ryan, R. M., Carland, J. E., Imlach, W. L., and Christie, M. J. (2014) Glycine transport inhibitors for the treatment of pain. *Trends Pharmacol. Sci.* **35**, 423–430
- Xu, T.-X., Gong, N., and Xu, T.-L. (2005) Inhibitors of GlyT1 and GlyT2 differentially modulate inhibitory transmission. *Neuroreport* **16**, 1227–1231
- Mostyn, S. N., Sarker, S., Muthuraman, P., Raja, A., Shimmon, S., Rawling, T., Cioffi, C. L., and Vandenberg, R. J. (2020) Photoswitchable ORG25543 congener enables optical control of glycine transporter 2. *ACS Chem. Neurosci.* **11**, 1250–1258
- Mostyn, S. N., Carland, J. E., Shimmon, S., Ryan, R. M., Rawling, T., and Vandenberg, R. J. (2017) Synthesis and characterization of novel acylglycine inhibitors of GlyT2. *ACS Chem. Neurosci.* **8**, 1949–1959
- Mostyn, S. N., Rawling, T., Mohammadi, S., Shimmon, S., Frangos, Z. J., Sarker, S., Yousuf, A., Vetter, I., Ryan, R. M., Christie, M. J., and Vandenberg, R. J. (2019) Development of an N-acyl amino acid that selectively inhibits the glycine transporter 2 to produce analgesia in a rat model of chronic pain. *J. Med. Chem.* **62**, 2466–2484
- Vandenberg, R. J., Mostyn, S. N., Carland, J. E., and Ryan, R. M. (2016) Glycine transporter2 inhibitors: Getting the balance right. *Neurochem. Int.* **98**, 89–93
- Subramanian, N., Scopelitti, A. J., Carland, J. E., Ryan, R. M., O'Mara, M. L., and Vandenberg, R. J. (2016) Identification of a 3rd Na<sup>+</sup> binding site of the Glycine transporter, GlyT2. *PLoS One* **11**, e0157583
- Carland, J. E., Thomas, M., Mostyn, S. N., Subramanian, N., O'Mara, M. L., Ryan, R. M., and Vandenberg, R. J. (2017) Molecular determinants for substrate interactions with the glycine transporter GlyT2. *ACS Chem. Neurosci.* **9**, 603–614
- Forrest, L. R., Zhang, Y.-W., Jacobs, M. T., Gesmonde, J., Xie, L., Honig, B. H., and Rudnick, G. (2008) Mechanism for alternating access in neurotransmitter transporters. *Proc. Natl. Acad. Sci. U. S. A.* **105**, 10338–10343
- Krishnamurthy, H., and Gouaux, E. (2012) X-ray structures of LeuT in substrate-free outward-open and apo inward-open states. *Nature* **481**, 469–474
- Zeppelin, T., Ladefoged, L. K., Sinning, S., Periole, X., and Schiott, B. (2018) A direct interaction of cholesterol with the dopamine transporter prevents its out-to-inward transition. *PLoS Comp. Biol.* **14**, e1005907
- Hurst, D. P., Grossfield, A., Lynch, D. L., Feller, S., Romo, T. D., Gawrisch, K., Pitman, M. C., and Reggio, P. H. (2010) A lipid pathway for ligand binding is necessary for a cannabinoid G protein-coupled receptor. *J. Biol. Chem.* **285**, 17954–17964
- Hua, T., Vemuri, K., Pu, M., Qu, L., Han, G. W., Wu, Y., Zhao, S., Shui, W., Li, S., Korde, A., Laprairie, R. B., Stahl, E. L., Ho, J. H., Zvonok, N., Zhou, H., et al. (2016) Crystal structure of the human cannabinoid receptor CB1. *Cell* **167**, 750–762.e714
- Hanson, M. A., Roth, C. B., Jo, E., Griffith, M. T., Scott, F. L., Reinhart, G., Desale, H., Clemons, B., Cahalan, S. M., Schuerer, S. C., Sanna, M. G.,

## Bioactive lipid inhibitors of glycine transporter 2

- Han, G. W., Kuhn, P., Rosen, H., and Stevens, R. C. (2012) Crystal structure of a lipid G protein-coupled receptor. *Science* **335**, 851–855
23. Bai, J. Y., Ding, W. G., Kojima, A., Seto, T., and Matsuura, H. (2015) Putative binding sites for arachidonic acid on the human cardiac Kv 1.5 channel. *Br. J. Pharmacol.* **172**, 5281–5292
24. Trott, O., and Olson, A. J. (2010) AutoDock vina: Improving the speed and accuracy of docking with a new scoring function, efficient optimization, and multithreading. *J. Comput. Chem.* **31**, 455–461
25. Stroet, M., Caron, B., Visscher, K. M., Geerke, D. P., Malde, A. K., and Mark, A. E. (2018) Automated topology builder version 3.0: Prediction of solvation free enthalpies in water and hexane. *J. Chem. Theor. Comput.* **14**, 5834–5845
26. Van Der Spoel, D., Lindahl, E., Hess, B., Groenhof, G., Mark, A. E., and Berendsen, H. J. (2005) GROMACS: Fast, flexible, and free. *J. Comput. Chem.* **26**, 1701–1718
27. Schmid, N., Eichenberger, A. P., Choutko, A., Riniker, S., Winger, M., Mark, A. E., and van Gunsteren, W. F. (2011) Definition and testing of the GROMOS force-field versions 54A7 and 54B7. *Eur. Biophys. J.* **40**, 843
28. Humphrey, W., Dalke, A., and Schulten, K. (1996) VMD: Visual molecular dynamics. *J. Mol. Graph.* **14**, 33–38